Variable Frequency VLF Signals In The Magnetosphere: Associated Phenomena and Plasma Diagnostics

C. R. CARLSON, R. A. HELLIWELL, AND D. L. CARPENTER

Space, Telecommunications, and Radioscience Laboratory, Stanford University, California

Coherent variable frequency signals (ramps) extending from 1 to 8 kHz, injected into the magnetosphere from Siple Station, Antarctica ($L=4.3$) exhibit upper and lower cutoffs when received at the conjugate station, Roberval, Quebec. Ramp group delay measurements and ionospheric sounding data are used for the first time to determine the cold plasma density and L shell of the propagation path. Relationships among f, df/dt, and the "phase equator" for gyroresonance are calculated using second-order resonance equations generalized to relativistic electrons. Observed upper cutoff characteristics are interpreted in terms of off-equatorial gyroresonant interaction regions and ducted propagation limited to frequencies below half the local gyrofrequency. The observed lower cutoff frequencies varied systematically with transmitted ramp slope, suggesting a threshold in the resonant electron number density above which rapid temporal wave growth and saturation can occur. This concept is used to develop a hot plasma diagnostic technique which, for an assumed $g(\alpha)v^{-n}$ electron distribution, provides an estimate of the energy dependence n. A test of this technique is given using the data and a simplified wave-particle interaction simulation. Additional aspects of the magnetospheric response to ramp injection, including emission triggering, are discussed.

1. INTRODUCTION

VLF transmitting experiments from Siple Station, Antarctica have revealed many features of the response of the magnetosphere to the injection of coherent waves [e.g., *Helliwell and Katsufrakis*, 1974, 1978; *Helliwell*, 1983a, b]. For reasons of simplicity in both data analysis and interpretation, attention was initially focused upon constant frequency transmissions. More recently, swept frequency signals called "ramps" have been employed to investigate frequency-dependent propagation effects such as the half gyrofrequency upper cutoff and wave growth as a function of ramp slope. In this paper we consider a case of ramp transmissions in which the observed signals were exceptionally well defined.

A schematic diagram of the experiment, showing frequency-time curves of four frequency ramps extending from 1 to 8 kHz, is given in Figure 1. Figure 1a shows the ramps as transmitted from Siple. To the right is the estimated radiated power as a function of frequency. Figure 1b shows typical frequency-time curves of the ramps as received at Roberval, Canada. To the right is a curve showing characteristic features of the signal level versus frequency for all but the steepest ramps. These signals are inferred to have propagated from Siple to Roberval along one or more geomagnetic field-aligned ducts of enhanced ionization. Several important features of the received ramps are identified by numbers, as follows:

1) Curvature due to dispersion. This feature is used for the first time to estimate the L shell and equatorial electron density of the propagation path, information usually extracted from whistlers [*Carpenter and Miller*, 1976].

2) A low-frequency amplitude cutoff, corresponding to the onset of rapid growth (decay) on rising (falling) ramps. This frequency is found to vary with ramp slope in a way that

suggests its use as a hot plasma diagnostic. The theory and application of such a diagnostic are discussed.

3) Amplitude saturation, following growth on the more gradual ramps.

4) Triggered emissions. Several types were present, including the indicated rising emissions triggered by the more gradual ramps.

5) A high-frequency amplitude cutoff, interpreted as a half gyrofrequency cutoff effect for whistler mode propagation in ducts of enhanced ionization [*Smith*, 1961; *Carpenter*, 1968]. Its variation with slope is found to be consistent with off-equatorial locations for wave growth.

Spectrograms of the primary data set, received at Roberval between 1436 and 1441 UT on September 12, 1979, are shown in Figure 2. Preceding the received ramps, above and below the spectra, are sloping tick marks. When lines are drawn through the tick mark pairs, these define the ramps as transmitted over the range 1 to 8 kHz with positive and negative slopes of 7, 3.5, 2, 1.75, 1.4, 1, 0.5, 0.25, and 0.125 kHz/s. An identical format transmitted 15 min earlier (1421–1426 UT) was also analyzed. These data sets exhibited a number of qualities favorable for signal analysis, including acceptable levels of sferics, hiss, and power line interference. Major features of the ramps in Figure 2 were repeated in the earlier data set (1421–1426 UT) and on ramps transmitted on other days, suggesting that temporal changes in the propagation medium, within the 5 min of transmission, were not significant.

The transmitting facility is a tunable system whose resonant frequency f_t is controlled by adding series impedance. Added inductance decreases f_t below the natural $\sim$5-kHz resonant frequency of the 21-km dipole antenna, increasing the energy storage capacity (the Q) and narrowing the bandwidth of the system. This effect is illustrated in Figure 3, which shows radiated power versus frequency for three different resonant frequencies, normalized by the power delivered to the antenna at f_t. The normalized power profiles are based in part upon measurements of rms current input to the antenna and the antenna resistance, both of which are
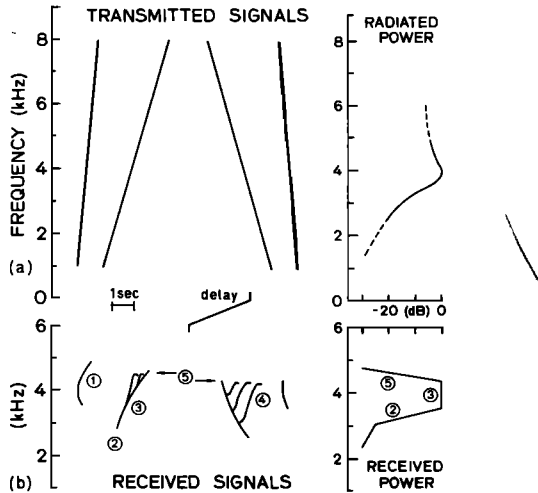
Fig. 1. Simplified sketch of frequency versus time spectra identifying the main features of the data analyzed in this research. The top panel (a) shows rising and falling ramps, extending from 1 to 8 kHz, as transmitted from Siple Station, Antarctica, with the estimated radiated power plotted to the right. The bottom panel (b) shows characteristic frequency-time curves of the ramps as received at Roberval, Canada, with the characteristic amplitude features of the received signals plotted to the right. The circled numbers 1 through 5 indicate dispersion, lower cutoff, saturaton, emissions, and upper cutoff, respectively.

Fig. 3. Radiated power characteristics of the Siple VLF transmitting system (21 km dipole antenna). The solid curves show the estimated power radiated for three different resonant frequencies f_t, normalized by the power delivered to the antenna at each f_t. The dashed curve is the radiation efficiency.

frequency dependent. The curve drawn through the peaks of the radiated power profiles is the antenna radiation efficiency derived by Raghuram et al., [1974]. Rocket borne wave measurements at 3.85 kHz over Siple [Kintner et al., 1983] gave an efficiency within a factor of two of the corresponding value given in Figure 3. The profile for $f_t = 3.97$

kHz in Figure 3 corresponds to the present data set, for which the peak input power was ~60 kW.

Amplitude measurements of the received signals were obtained with a frequency tracking filter. Because of rise time limitations, a 300-Hz-wide bandpass filter was used for the ramps with slope magnitudes >1 kHz/s. For less steep ramps a 100-Hz filter was used to improve the output signal-to-noise ratio. The difference in amplitude measurements when both filters were applied to the same ramp was less than 1 dB.
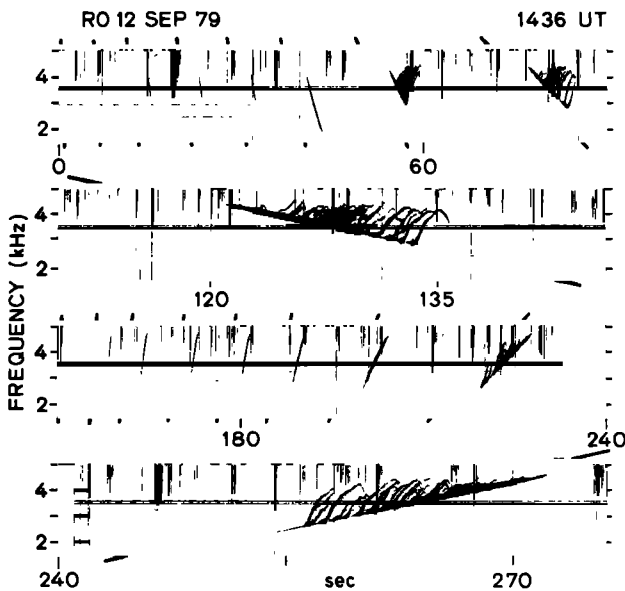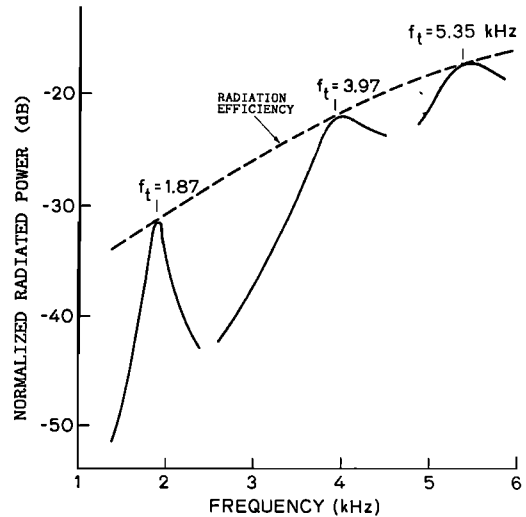

Fig. 2. Spectra of VLF frequency ramps transmitted from Siple, Antarctica, as received at Roberval, Canada, on September 12, 1979. Rising and falling ramps were transmitted with ramp slope magnitudes ranging from 7 to 0.125 kHz/s. Sloping tick marks preceding each ramp, above and below the spectra, indicate the transmitted slope (vertical tick marks show time).
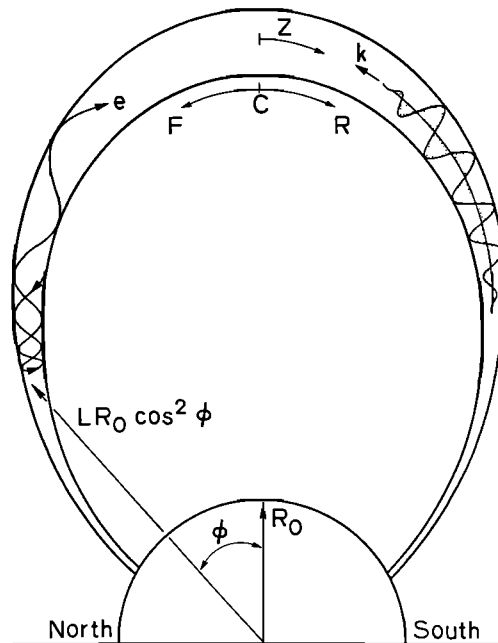

Fig. 4. Sketch of field line at $L = 4$, showing the location with respect to the magnetic equator of the postulated interaction region, or phase equator, of constant (C), rising (R), and falling (F) frequency signals. Also defined are field position z, geomagnetic latitude ϕ, and the relationship between the radial distance and ϕ for a dipole field.
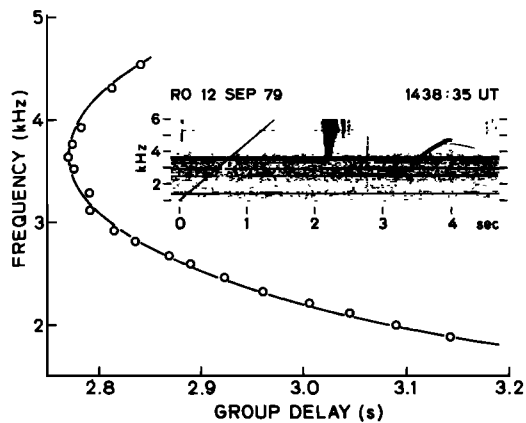
Fig. 5. Inset shows the spectra of a received ramp near $t=4$ s. The corresponding 3.5-kHz/s transmitted ramp (sloping straight line) is shown beginning at $t=0$ s. Circles and a solid curve show the measured and theoretical frequency versus group delay, respectively.

Our interpretation of the data is based on the premise that the location of the principal wave-particle interaction region ("phase equator") is a function of ramp slope. This model, as is sketched in Figure 4, places the center of the interaction region on the magnetic equator for constant frequency signals (C) and upstream or downstream of the equator for falling (F) or rising (R) signal frequencies, respectively [Helliwell, 1967]. The phase equator concept is used in later sections to interpret growth and cutoff features of the data and underlies a new method for ground based hot plasma diagnostics.

2. PATH ANALYSIS AND COLD PLASMA DIAGNOSTICS

The common procedure in path analysis is to compare the travel time of a Siple signal with travel times of simultaneously propagating multicomponent whistlers. If a whistler component and a Siple signal have the same travel times at a given frequency, they are assumed to have propagated within the same duct. The frequency-time curve of this whistler component is used to estimate the magnetic shell (L value) and equatorial cold plasma electron density of the path [Carpenter and Miller, 1976]. In the present case no measurable whistlers were present, and for the first time the dispersion of a Siple signal was used for path identification.

As is shown in Figure 5 (inset), the chosen ramp had a transmitted slope of 3.5 kHz/s and was detected between ~ 2.0 and 4.6 kHz, and had a frequency of minimum arrival time at ~ 2.3 kHz. The $f - t$ measurements, shown as open circles in Figure 5, give a minimum group delay t_n of 2.77 s at a "nose" frequency f_n of 3.65 kHz. Using these data, the path parameters $L \sim 4.53 \pm 0.02$ ($L \sim 4.3$ for Siple Station at 100 km altitude), equatorial gyrofrequency $f_{Heq} \simeq 9.4 \pm 0.1$ kHz, and equatorial cold plasma electron density $\sim 280 \pm 20$ el/cm^3 were estimated [Park, 1972]. These estimates are based on a diffusive equilibrium model of the cold plasma density along the path and an ionospheric electron content estimated using ionograms from Halley Station, Antarctica. These path parameters and the quiet magnetic conditions ($Kp = 1^+$ during the event and $Kp = 1, 1^-, 1^-$

during the 9 hours preceding the event) were typical of periods of good transmission from Siple to Roberval [Carpenter and Miller, 1976; Carpenter and Bao, 1983].

A theoretical whistler, shown by the solid curve in Figure 5, was calculated using these parameters and the Bernard [1973] approximation to the travel time integral. The measured frequencies lie within 0.01 s of the theoretical curve. An advantage of the Siple ramp is the known location and timing of the transmitted signal. Whistler sources are often difficult to identify, and even when known in time are usually not known in geographic location. Accordingly, group delay measurements from frequency ramps are inherently more accurate than those from whistlers.

Most of the discussion of the data in this paper assumes a single dominant propagation path. However, there is evidence suggesting the occurrence of both propagation on separate paths with similar travel times, as well as multimode propagation within a single duct [Scarabucci and Smith, 1971]. Evidence for propagation on separate paths includes falling tone emissions crossing over rising tone emissions without apparent interaction [Helliwell and Katsufrakis, 1978; Helliwell, 1979] and nearly periodic amplitude fluctuations suggesting beating between ramps with slightly different group delays.

3. EXPERIMENTAL RESULTS: KEY FEATURES

Although transmitted between 1 and 8 kHz, the frequency ramps of interest were generally detected only between ~ 2 and ~ 5 kHz. Spectrograms and amplitude-time profiles of the upper and lower cutoff regions are given in Figures 6 and 7, respectively, for the 1436—1441 UT data set. The time axes have been aligned so that spectrographic features of the ramps correlate vertically with the amplitude features.

The development of a typical ramp includes an initial rise above the background noise level, followed by exponential-like rapid intensity growth (greater than 40 dB/s), which lasts until the amplitude saturates [Helliwell and Katsufrakis, 1974] or begins to decay. For ramp slope magnitudes < 1 kHz/s the grown signal tends to rise in frequency above the input signal, becoming a rising emission (see section 7). The ramp is described as being in saturation if, following a period of growth, changes in frequency and hence radiated power (see Figure 3) are not accompanied by proportional changes in received intensity. Each grown signal then experiences an exponentiallike rapid intensity decay (faster than −60 dB/s) and eventually drops below the background noise level. Features which characterize the general amplitude profile of a ramp have been selected. The frequencies corresponding to these features have been measured and are defined below:

f_{-25dB}: frequency at which the received intensity passed through a value 25 dB below 10 μV/m (the −25-dB level was chosen as the lowest level at which all ramps could be detected on the amplitude profiles);

f_{RG}, f_{RD}: frequencies at the onset of exponentiallike rapid intensity growth and decay, respectively;

f_{SH}, f_{SL}: upper and lower frequency limit of saturation behavior, respectively.

These features are identified in Figures 6 and 7 by subscripted frequencies and symbols (above and below the am-
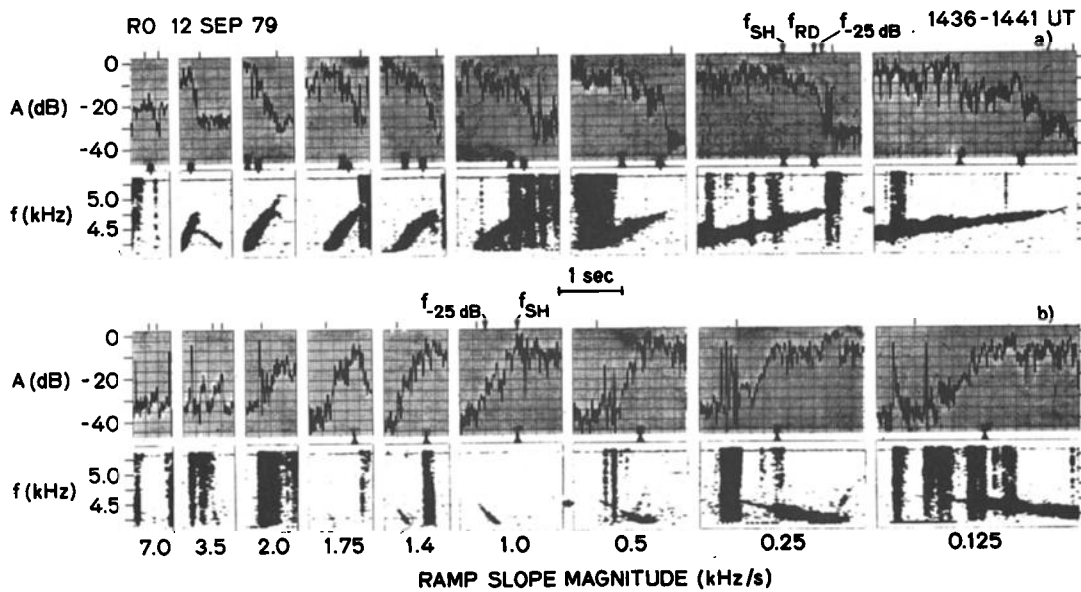
Fig. 6. Amplitude versus time and spectra of the upper intensity cutoff for both the rising (a) and falling (b) ramps shown in Figure 2. The amplitude profiles were obtained using a narrowband frequency tracking filter which locked onto or unlocked from the received signal coincident with a tick mark above the amplitude plots. The parameters f_{SH}, f_{RD}, and f_{-25dB} are indicated above representative amplitude plots, f_{max} is indicated to the side of the corresponding spectra, and symbols for f_{SH} and f_{RD} are indicated below each amplitude plot. These refer to characteristic amplitude features whose frequencies are shown in Figure 8.

plitude plots, respectively) and are plotted in Figure 8 versus ramp slope for both data sets. There are errors associated with the identification of the measured quantities, the largest tending to be in f_{SL} and f_{SH}. For the falling ramps, f_{RG} was not measured, since rapid growth apparently began at signal amplitudes below the observed noise levels. In Figure 8, the top and bottom thin-line regions represent the upper and lower cutoff regions, respectively, while the thick-line regions represent saturation.
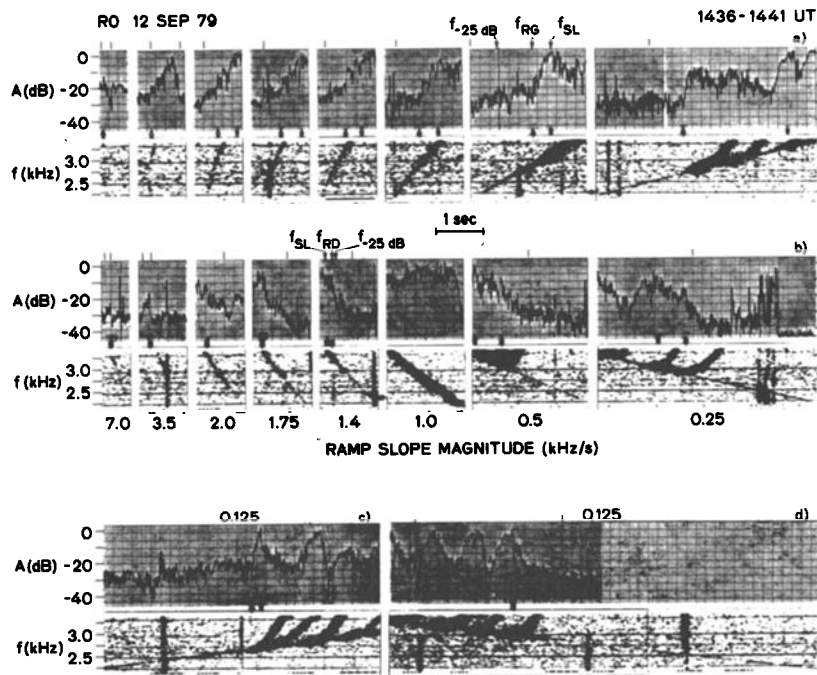
On the 1421−1426 UT data set the ±7-, −3.5-, and −2-

Fig. 7. Amplitude versus time and spectra of the lower intensity cutoff for both the rising (a and c) and falling (b and d) ramps shown in Figure 2, analogous to Figure 6. The parameters f_{-25dB}, f_{RG}, f_{SL}, and f_{RD} are indicated above representative amplitude plots; f_{min} is indicated beside the corresponding spectra; and symbols for f_{RG}, f_{SL}, and f_{RD} appear below each amplitude plot. These refer to characteristic amplitude features whose frequencies are shown in Figure 8.

kHz/s ramps were not detected on the spectra, suggesting that these were cases of little or no wave growth. The ramps which did show growth but did not attain saturation, as indicated in Figure 8, experienced decay before saturation was achieved. The 3.5-kHz/s ramp on the 1421−1426 UT data set showed no evidence of exponentiallike rapid intensity growth.

Low-Frequency Cutoff

The lower cutoff, summarized in Figure 8, occurs during decay for the falling ramps and growth for the rising ramps. A key point is that while the lowest frequencies at which signals could be recognized on the spectrograms did not vary systematically with ramp slope, f_{RG} and f_{RD} tended to increase with ramp steepness. The −1-kHz/s ramps, which extended to anomalously low frequencies and triggered "falling" emissions, were exceptions and are discussed later. In both data sets, rapid decay on the −0.5-, −0.25-, and −0.125-kHz/s ramps occurred when a triggered rising emission left the tracking filter passband and there was no following regrowth of the ramp (see Figure 7d).

High-Frequency Cutoff

Upper cutoff occurs during growth for the falling ramps and decay for the rising ramps. The extreme limits of detection of the rising ramps exceeded those of the falling ramps by ∼100 Hz. As the ramp slope was changed from −7 to +7 kHz/s, f_{-25dB} and f_{SH} tended to increase, while the highest frequencies at which signals could be recognized on

Fig. 9. Derived amplitude versus frequency curves for the upper cutoff portion of the rising ramps shown in Figure 6. The dashed curve shows the amplitude rolloff of a whistler from another period which propagated on a path similar to that of the ramps.

the spectrograms tended to remain relatively constant near ∼4.6 kHz.

Derived amplitude versus frequency curves for the rising ramps, shown in Figure 9, do not depend strongly upon ramp slope, with the exception of the 7-kHz/s ramp, which is believed to have reached cutoff during growth. The dashed curve shows the upper cutoff rolloff of a whistler with path parameters similar to those of the ramps [Carpenter, 1968].

Section 7 contains a review and discussion of data features which are relevant to the study of frequency ramps but which are not fundamental to the following discussion, in three sections, of gyroresonance relations.

4. SECOND-ORDER GYRORESONANCE RELATIONS

This section examines the theory of gyroresonant interactions involving variable frequency signals. In the following section, the theory is applied to the data and the observed ramp slope dependences.

The interaction model developed by Helliwell [1967] predicts that the length of the wave-particle interaction region will maximize at the phase equator of the applied signal and the counterstreaming electrons. To visualize this mechanism, assume adiabatic electron motion and let the gyrophase ψ be the angle between the wave's magnetic field and the electron perpendicular velocity. When $d\psi/dt = 0$, the wave and the electron are in first order resonance. The effective length of resonance will maximize when $d^2\psi/dt^2 = 0$, which is called the second-order resonance condition. For a given electron, the point where $d^2\psi/dt^2 = 0$ depends on the local change in wave frequency with time, $\partial f/\partial t$. For pitch angles < 30° the variations of the gyrophase with distance along the field line from this point are, to first order, independent of the location of this point, and hence of $\partial f/\partial t$ [Helliwell, 1970]. For this reason, the point where $d^2\psi/dt^2 = 0$ has also been called the phase equator.

At a given point the relativistic condition for first order resonance is

$$v_\parallel \simeq v_R = \frac{2\pi\left(\frac{f_H}{\gamma} - f\right)}{k} \qquad (1)$$

assuming longitudinal propagation. The second-order resonance condition will be satisfied if the variation of the electron parallel velocity $v_\parallel$ along the electron orbit is matched by the variation of v_R.

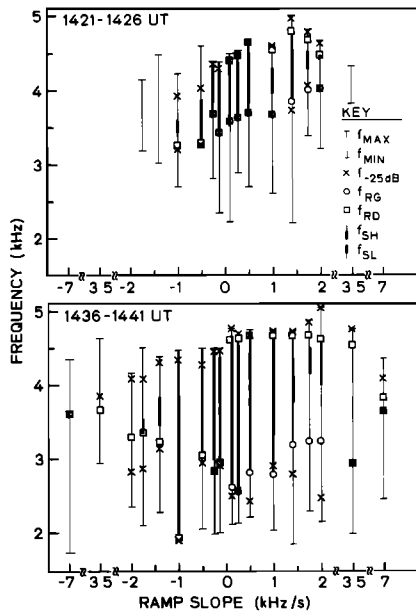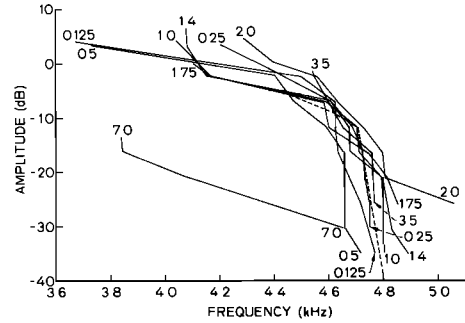The equations describing the required time variation of

Fig. 8. Frequencies associated with amplitude features of the received ramps shown in Figure 2 and for identical ramps transmitted 15 minutes earlier (upper plot). The parameters f_{max} and f_{min} are the highest and lowest frequencies at which the received ramps were detected on spectra, respectively; f_{-25dB} is the frequency at the signal's −25 dB level; f_{RD} and f_{RG} are the frequencies at the onset of rapid decay and growth, respectively; and f_{SH} and f_{SL} are the high and low frequency limits of the saturation region, respectively. The upper frequency thin-line, thick-line, and lower frequency thin-line sections represent the upper cutoff, saturation, and lower cutoff regions, respectively. The parenthisized symbols in the key refer to the notation used in Figures 6 and 7.
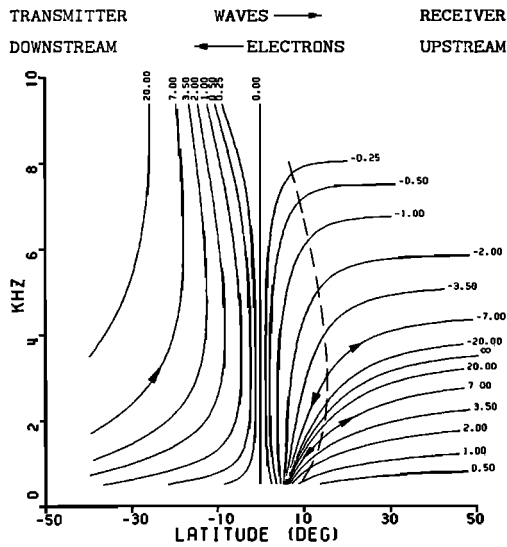
Fig. 10. Frequency versus latitude of the phase equator for 30° pitch angle electrons, parametric in ramp slope (kHz/s). The latitude is measured from the magnetic equator as shown in Figure 4. The second phase equator for rising ramps at low frequencies is a consequence of the dispersion of the rising transmitted signal into a falling signal. The arrows indicate the directions of changes with time. The dashed curve shows the locus of frequencies and latitudes where the phase equator splits, one phase equator moving up in frequency with time and the other moving down.

frequency for second-order resonance $[\partial f/\partial t]_{res}$, generalized to relativistic electrons and for longitudinal propagation, are developed in the appendix. Relationships associated with the solution to the second-order resonance condition, assuming a dipole field model, a diffusive equilibrium cold plasma distribution, adiabatic invariance of the electron motion, and 30° pitch angle electrons, are shown in Figures 10, 11, and 12. In each figure the upstream or downstream label indicates where the phase equator is located with respect to the magnetic equator and the counterstreaming electrons. Since the transmitter is located in the south, upstream and downstream phase equator loca-

tions also imply positive (northern) and negative (southern) phase equator latitudes, respectively.

Curves of frequency versus phase equator latitude, parametric in transmitted ramp slope, are given in Figure 10. Figure 11 relates frequency at the phase equator to the total energy of the resonant electrons. In general, the resonant electron energy increases as the frequency decreases. As the ramp slope magnitude increases at a fixed frequency, both the resonant energy (Figure 11) and the magnitude of the phase equator latitude (Figure 10) increase.

Magnetospheric dispersion increases the group delay at the upper and lower frequency limits of the ramps (the nose frequency effect). As is illustrated in Figure 1 (bottom left) the lower frequency ends of rising ramps tend to be dispersed into falling tones (e.g., see inset in Figure 5) and the upper frequency ends of falling ramps tend to be dispersed into rising tones. The extent in frequency of the ramp segments for which the slope changes sign depends upon ramp slope, being large for the steeper slopes. Thus in Figure 10, the rising ramps have phase equators in the south as expected, and after propagating across the equator, have additional phase equators for the low frequency segments which have changed into falling tones. For example, near 2 kHz on the 7-kHz/s ramp, the initial phase equator should be located near −35° geomagnetic latitude and involve electrons of energy > 100 keV (Figures 10 and 11). The second phase equator should be located near 20° geomagnetic latitude and involve ~10-keV electrons (the second interaction could produce more wave growth than the first due to higher resonant electron number densities). The corresponding high-frequency effect on falling ramps is different, as these ramps do not in general have rising tone phase equators in the south. There is a high frequency limit of the phase equator range in the north (Figure 10), just below the nose (slope reversal) frequency for each ramp.

The directions in which the phase equator frequency and latitude move with time are indicated in Figure 10 by arrows on the ±7-kHz/s curves. For rising tones (downstream), the initial phase equator is also the lowest frequency phase equator, and the phase equator frequency increases with time. As time advances, the phase equator moves toward the equator
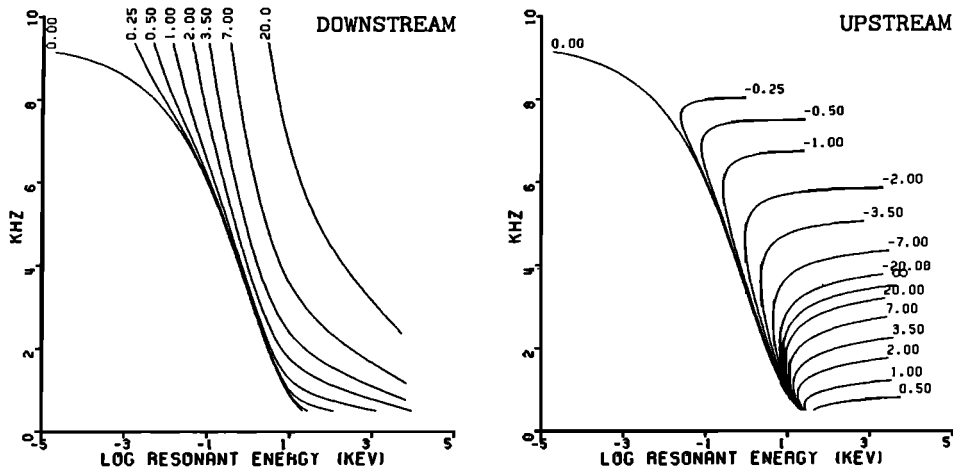

Fig. 11. Frequency versus resonant electron energy for second-order resonant, 30° pitch angle electrons, parametric in ramp slope. The left and right panels give the energies for downstream and upstream phase equators, respectively.
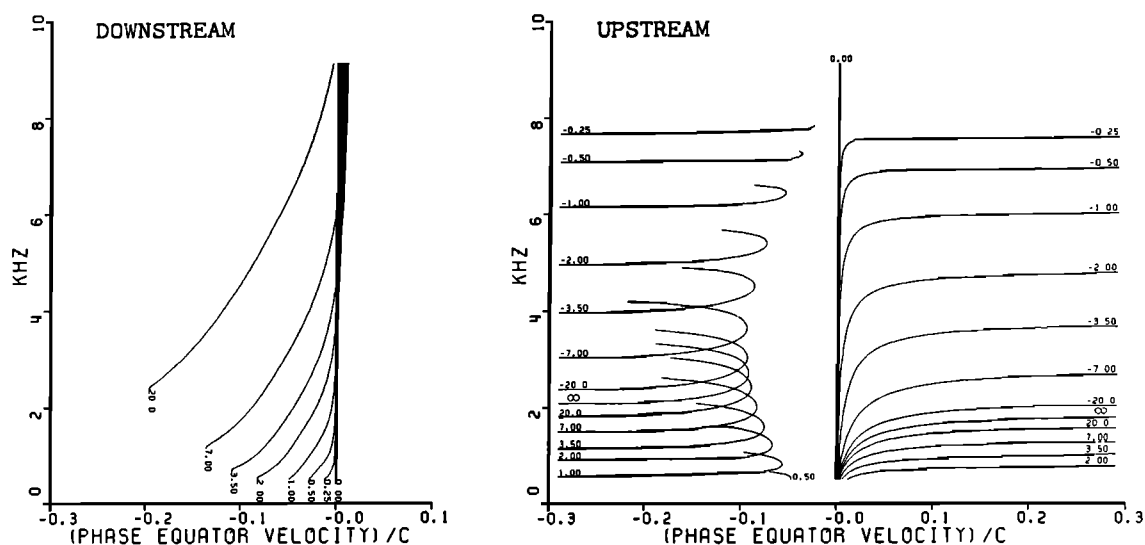
Fig. 12. Frequency versus phase equator velocity for 30° pitch angle electrons, parametric in ramp slope. This is the velocity associated with the change in phase equator location with time. The left and right panels give the phase equator velocities for downstream and upstream phase equators, respectively.

and then away again. However, for falling tones (upstream), second-order resonance initially occurs at some intermediate frequency on the falling tone segment. Hence there is a "splitting" effect, with one phase equator moving to higher frequencies and latitudes with time and the other to lower frequencies and latitudes. The dashed curve shows the locus of the frequencies and latitudes where the phase equator "splits." The splitting concept is discussed further in a later paragraph.

Figures 10 through 12 include the second-order resonance solution for constant frequency signals (slope=0) and for an impulse (slope=∞). Although a downstream phase equator is not shown for an impulse, one will exist for high pitch angle electrons ($\alpha > 80°$) and for frequencies generally above the equatorial half gyrofrequency.

For falling tones, electrons of a given α and $v_{\parallel}$ may be in second-order resonance with the same ramp at two different frequencies due to the occurrence of a minimum in the resonant electron energy at an intermediate ramp frequency (Figure 11, right panel). This minimum develops because resonant energy increases with decreasing frequency and also with increasing latitude magnitude. In the upstream case, the latitude magnitude is greatest at the high frequency end of the second-order resonance curves (Figure 10) where, as noted above, dispersion leads to slope reversal.

The foregoing discussion was based upon calculations for a given pitch angle. The consideration of all pitch angles results in a spread of phase equator locations, and the width of this spread increases with ramp steepness. For larger pitch angles but for the same frequency and transmitted slope, the second-order resonance condition is satisfied nearer the equator (the total resonant electron energy will then be greater, even though the parallel velocities will be less as required by the resonance condition (1)). In this respect ramps differ from constant frequency signals, for which the phase equators for all pitch angles are located at the magnetic equator.

The pitch angle dependence of the phase equator location

also leads to an asymmetry between rising and falling ramps when considering the total wave-particle interaction. For a rising ramp and second-order resonant electrons, the radiation generated by the lower pitch angle electrons will propagate toward the equator and be seen by the higher pitch angle electrons. The reverse will be true for falling ramps, while for constant frequency signals all second-order resonant electrons will see the radiation previously generated by all other second-order resonant electrons. The spreading of the phase equator locations with ramp steepness and the associated asymmetry in the "feedback" of radiation may be related to observable features in the data, but will not be pursued in this paper.

Because of dispersion and because the transmitted frequency is changing with time, the dipole latitude of the phase equator varies with time, and hence ramp frequency. This motion of the phase equator has a velocity given by

$$v_{pe} = \frac{dz_{pe}}{dt} \qquad (2)$$

where z_{pe} represents the phase equator location. Curves of v_{pe} versus frequency, parametric in ramp slope, are given in Figure 12. Dispersed ramps having a high $\partial^2 f/\partial t^2$ can have phase equator velocities greater than the electron or wave velocities. This is related to a splitting of the phase equator for falling ramps and for the falling tone portions of initially rising ramps (Figure 10), and is shown in Figure 12 by discontinuous singularities in the v_{pe} curves. For a given ramp this discontinuity corresponds to the frequency at which the second-order resonance condition is first satisfied, as is indicated by the dashed curve in Figure 10. At the instant of the split the two v_{pe}'s are infinite and opposite in sign, one phase equator moving up in frequency with time (negative v_{pe}) and the other moving down in frequency with time (positive v_{pe}). In order for the phase equator to move up in frequency while the local frequency is dropping, v_{pe} must be in the direction of the group velocity and exceed the latter in magnitude.
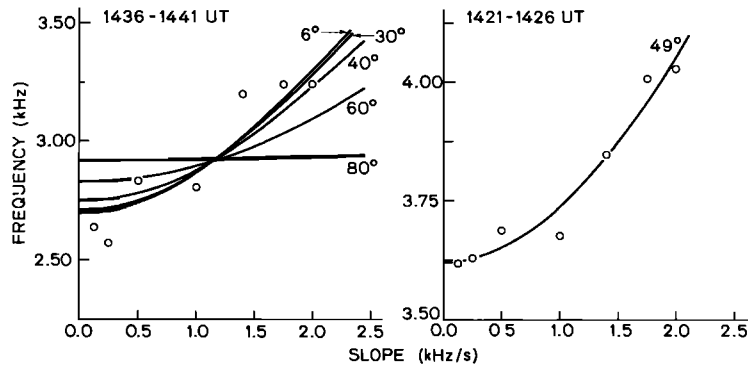
Fig. 13. Curves of frequency at the point of second-order resonance versus transmitted ramp slope calculated for constant values of pitch angle and electron parallel velocity. The circles represent the observed onsets of rapid intensity growth at frequency f_{RG} on the rising ramps shown in Figure 2 (left panel) and on the rising ramps of an earlier data set (right panel). Their fit with the curves is consistent with a model involving a threshold resonant electron number density for wave growth.

The higher velocities indicated demonstrate that the phase equator velocity is in a sense nonphysical in nature, by analogy to the phenomenon of wave phase velocity. The higher phase equator velocities generally occur outside the observed range of the data, with some exceptions mentioned later. It seems possible that high phase equator velocities could affect the coherent addition of the radiation stimulated by resonant electrons and an applied signal.

5. LOWER CUTOFF INTERPRETATION: AN APPROACH TO A HOT PLASMA DIAGNOSTIC

In the lower intensity cutoff data of Figures 7 and 8, the rapid amplitude changes at f_{RG} and f_{RD} are believed to be evidence of the power threshold for transition to exponential temporal growth reported by Helliwell et al. [1980]. Two mechanisms were suggested to explain this power threshold, which was previously measured by varying transmitter power at constant frequency. The first requires that for rapid growth, the applied signal level must exceed the plasmaspheric hiss level. The second requires the applied signal level to be large enough so that the phase shifts in the phase bunched currents, introduced by the inhomogeneity of the medium, are altered sufficiently to permit rapid growth. To first order however, the inhomogeneity and plasmaspheric hiss level do not change with phase equator location and thus cannot explain the ramp slope dependence of f_{RG} and f_{RD}. Thus we suggest that in conjunction with a smooth increase in radiated power with frequency (Figure 3), the dominant factor in the present case was an increase in the number density of resonant electrons with increasing frequency (or decreasing electron energy). As the number density increases, so should the growth component of the stimulated magnetic field (i.e., the stimulated magnetic field component in the direction of the applied magnetic field). Therefore it seems possible that at f_{RG} and f_{RD}, the growth component passed through threshold values for transition to exponential temporal growth or from saturated growth, respectively. This model can account for the increase in f_{RG} and f_{RD} with ramp slope magnitude. The effect is demonstrated in Figure 11, which shows that for a constant resonant electron energy and pitch angle, the second-order resonance frequency increases with ramp steepness.

Our interpretation of the lower cutoff suggests an approach to a hot plasma diagnostic technique. The ramp-slope variation of f_{RG} and f_{RD} is expected to depend upon the energetic electron distribution function. Therefore if wave-particle interactions were simulated using a given electron distribution, f_{RG} and f_{RD} values would be predicted from a threshold value of the stimulated growth component. If the distribution were taken to be of the form v^{-n}, a diagnostic for n could be obtained by fitting to the actual data the results of a series of simulations using various values of n. This plasma diagnostic technique suggests that a "full simulation" be performed, which would calculate the fields stimulated by the evolution of a full distribution of electrons in a propagating variable frequency wave field.

To test and visualize this technique, consider a simplified model. Assume that the effects of the actual interacting electrons can be represented by the second-order resonant electrons with pitch angles at some $\alpha = \alpha_{max}$, for which the growth component of the stimulated magnetic field per unit pitch angle $B_{sx}(\alpha)$, is maximized. Suppose further that there is a second-order resonant electron number density, and hence a value of $B_{sx}(\alpha_{max})$, above which rapid gyroresonant wave growth can occur and that within a Δv and $\Delta \alpha$ range, the number density is invariant with latitude. This threshold value of the resonant electron number density will correspond to some value of $v_{\parallel}$, which is then itself invariant with latitude. The invariance holds to first order even for anisotropic distribution functions, since near the equator and for the pitch angles of interest (discussed later) the distribution function is not strongly dependent upon latitude. The change in the number density due to the convergence of the earths magnetic field should be less than $\sim$10% for latitudes $< 10°$ magnitude. For the purpose of presenting a simple demonstration, these assumptions appear justified.

The first part of the diagnostic procedure consists of finding a best fit value of resonant electron pitch angle α. As an illustration, such a fit would occur for the $\alpha = 30°$ used to prepare Figure 11 if the observed values of f_{RG}, when plotted on their corresponding ramp slope curves, were arranged in a line above some equivalent value of $v_{\parallel}$. In practice, the f_{RG} values are used to estimate a best fit $v_{\parallel}$ for each α, and curves of second-order resonance frequency versus ramp slope, parametric in α, are compared to the data. The curve

which gives a least squares best fit to the f_{RG} or f_{RD} data will also be the $B_{sx}(\alpha_{max})$ threshold curve and will give α_{max}. The value of n in the distribution function (for the assumed anisotropy) can then be inferred from simulations that predict values of α_{max} as a function of n.

Figure 13 shows the best fits for several pitch angles applied to the f_{RG}'s (with the 3.5- and 7-kHz/s values removed). Recall from the previous section that for a "pancake distribution" of high pitch angle electrons ($\alpha > 80°$), the second-order resonance condition should be satisfied near the equator. This distribution would not be expected to yield ramp slope dependent f_{RG}'s or f_{RD}'s, as is suggested by the $\alpha = 80°$ curve in Figure 13. A relatively good fit of the 1436–1441 UT f_{RG}'s (left panel) was achieved for pitch angles between $\sim 6°$ (loss cone) and $30°$ and corresponding energies between ~ 1.2 and ~ 1.7 keV ($v_\parallel \simeq 2.1 \times 10^7$ m/s). For the 1421–1426 UT f_{RG}'s (right panel), the least squares best fit curve is shown and represents ~ 1.4-keV electrons with pitch angles near $49°$ and $v_\parallel \simeq 1.4 \times 10^{7'}$ m/s. Figure 14 shows the best fit curve to the 1436–1441 UT f_{RD}'s (with the -1, -3.5, and -7 kHz/s values removed) and represents ~ 1.4-keV electrons with $\alpha \simeq 32°$ and $v_\parallel \simeq 1.9 \times 10^7$ m/s. The 1421 UT data set f_{RD}'s were not analyzed because of insufficient data.

To calculate the $B_{sx}(\alpha)$ curves for this simplified model we performed a simulation of the wave-particle interaction [Helliwell and Inan, 1982] between constant frequency signals and the second-order resonant electrons. A plot of the output $B_{sx}(\alpha)$ is inset in Figure 15 for the deduced path parameters, a 3-kHz applied signal with an intensity of 0.3 pT at all latitudes, and a v^{-5} distribution function. Figure 15 shows α_{max} versus n for isotropic and anisotropic distribution functions, both corresponding to actual measurements [Kimura et. al., 1983]. The values of n, where α_{max} corresponds to the best fit α's of Figures 13 and 14, can be read from Figure 15. The 1421–1426 UT data set

Fig. 15. Plots of α_{max} versus the spectral index n for two different pitch angle anisotropies $g(\alpha)$. α_{max} is the pitch angle of the second-order resonant electrons for which the growth component of the stimulated magnetic field per unit pitch angle B_{sx}, calculated at the interaction region output, is a maximum for electron distributions of the form $g(\alpha)v^{-n}$. The inset plot is an example of B_{sx} versus α for a v^{-5} distribution function. B_{sx} was determined using a simulation model [Helliwell and Inan, 1982].

predicts $\alpha_{max} = 49°$ and $n \simeq 5$ ($n \simeq 6$ for the anisotropic case). Taking $\alpha_{max} = 30°$, the 1436–1441 UT data set predicts $n \simeq 12$ ($n \simeq 13$ for the anisotropic case). OGO 3 satellite measurements of the differential energy spectrum at $L \simeq 5.5$ fit a $v^{-3\pm0.5}$ ($E^{-1\ 5}$) power law [Schield and Frank, 1970]. This $v^{-3\pm0.5}$ differential energy spectrum converts to a $v^{-5\pm0.5}$ distribution function [e.g., Chang, 1983a] or $n \simeq 5$, the same value of n given by the 1421–1426 UT data set.

A simulation in which all significant electrons are considered could give values of n different than those given above. Wave-particle interactions have been simulated by several workers (for a review, see Matsumoto [1979] or work by Helliwell and Inan [1982], Omura and Matsumoto [1982], Vomvoridis et. al. [1982], Hashimoto et. al. [1983], and Nunn [1984]). Presently, no interaction model is capable of performing the full simulation suggested above, mainly due to computer speed and memory limitations.

The steep ramps ($|df/dt| > 2$ kHz/s) were excluded from the diagnostic analysis because amplitude features suggest that steep falling ramps experienced rapid decay before saturation was achieved and that steep rising ramps may never have been in a mode of rapid "temporal" growth. Extrapolation of the curves in Figures 13 and 14 to steeper ramp slopes indicates that the growth and cutoff of these ramps do not fit the second-order resonance model. For these ramps, the growth could result primarily from first-order resonant "spatial" growth. The -1-kHz/s ramp was also omitted from the fitted data set because of its anomalously low f_{RD}.

The important pitch angles in this model ($\alpha_{max} < 50°$) are lower than the $50° - 70°$ pitch angles predicted by Nunn [1984]. Nunn however, considers only trapped electrons, which automatically eliminates the low pitch angle electrons from consideration when low applied field intensities are used. For our model the applied field (0.3 pT) is apparently below the level at which trapped electrons play an important role in the wave growth. Figure 15 suggests that the ramp slope dependence of a lower cutoff frequency
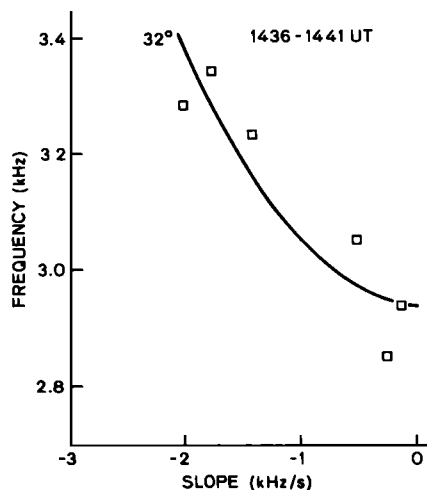

Fig. 14. Curves of second-order resonance frequency versus transmitted ramp slope for a constant pitch angle of $32°$ and constant electron parallel velocity. The squares represent the observed onset of rapid intensity decay at frequency f_{RD} on the falling ramps shown in Figure 2. Their fit with the curves is consistent with a model involving a threshold resonant electron number density for wave growth.
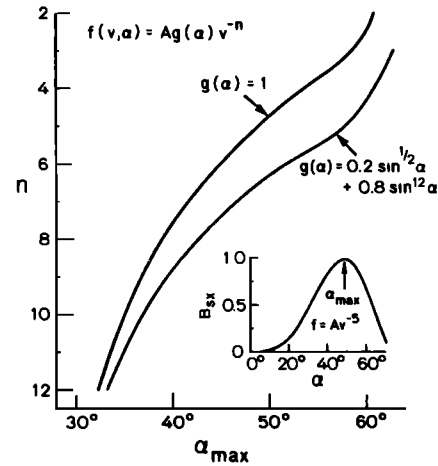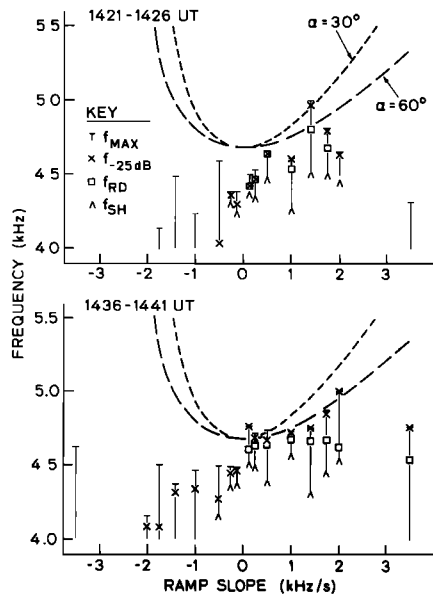
Fig. 16. Expanded portion of the upper cutoff region in Figure 8. The dashed curves are the calculated half gyrofrequency phase equators of transmitted ramps for 30° and 60° pitch angle electrons.

may be dominated by $\alpha > 50°$ electrons for hard ($n < 4$) distribution functions.

6. HIGH-FREQUENCY CUTOFF INTERPRETATION

The upper cutoff seems to be controlled primarily by the duct propagation cutoff at one half the electron gyrofrequency [Smith, 1961; Carpenter, 1968]. The frequency spread in the rising ramp f_{SH} values (Figure 8) reflects the previously noted subjectivity in their identification. The main point is that f_{SH} and f_{RD} are separated by a rolloff in intensity that does not vary in a simple way with frequency, time, or ramp slope. With increasing rising ramp slope f_{RD} and f_{-25dB} tended first to increase and then to decrease. This decrease at the higher slopes is believed to result from the ramp reaching cutoff before saturation. An expanded portion of the upper cutoff region in Figure 8 is given in Figure 16.

The falling ramp signal is interpreted as having been unducted at frequencies $f > f_{Heq}/2$, where $f_{Heq}/2$ was the approximate frequency at the beginning of the wave train as it entered the interaction region after crossing the equator. The falling ramps support this hypothesis; in the 1436–1441 UT data set, a common frequency of apparent growth onset was found at ~4.49 kHz, just below the estimated $f_{Heq}/2$ of 4.69 kHz. This onset frequency was determined by extrapolating the observed growth curves (such as in Figure 6b) into the noise, and finding a frequency at which the estimated amplitudes of all the ramps were nearly the same, ~ −36 dB below 10 $\mu V/m$. The previously mentioned splitting could influence the upper cutoff of the steeper ramps since, as shown by the dashed curve in Figure 10, the splitting can occur below the equatorial half gyrofrequency. Above the splitting frequency, v_{pe} is in the direction of and greater in magnitude than the group velocity, resulting in the phase equator moving up in frequency with time.

As mentioned earlier, the onset frequency for rapid decay

on the rising ramps was ~100 Hz above the onset frequency for growth on falling ramps. This suggests that the radiated power required to sustain the growth of a signal was often less than the radiated power necessary for the onset of exponential growth.

Rising ramps should encounter their second-order interaction regions prior to crossing the magnetic equator. The output of these regions would be expected to have relatively high amplitudes at frequencies up to the local half gyrofrequency. In Figure 16, dashed curves (for two pitch angles) show the relations between ramp slope and half gyrofrequency within calculated second-order interaction regions. The agreement between these curves and the observed rise in upper cutoff with ramp slope lends support to the second-order interaction model. However, the question of transequatorial propagation of ramp frequencies above $f_{Heq}/2$ must be considered.

Transequatorial propagation of signals with $f > f_{Heq}/2$ has been predicted to occur within a limited wave-normal-position window [Bernhardt, 1979]. Some ducting loss is also expected at frequencies below $f_{Heq}/2$. Therefore it seems possible that the pre-rapid decay rolloff on rising ramps beginning at f_{SH}, and the upper frequency limit on the observation of falling ramp signals (both ~200 Hz below the estimated $f_{Heq}/2$) are due to ducting losses during transequatorial propagation. In some cases the stimulated signal became free running, resulting in the appearance of the inverted hooks shown in Figure 6a. These emissions lasted less than 0.5 s and usually showed a negative d^2f/dt^2. These emissions and the rapid intensity decay could be associated with reduced input signal intensities due to ducting losses, thus causing a loss of control of the stimulated signal.

The appearance of multiple inverted hooks on the rising ramps could be a result of multipath propagation; however, there are other possible explanations. Single duct, multimode propagation predicted by a full wave treatment of ducted propagation [Scarabucci and Smith, 1971] suggests that higher-order modes with larger discrete wave normal angles would have lower upper cutoff frequencies and larger group delays above the nose frequency. If each mode had independent interactions, then triggering of multiple inverted hooks might occur along with frequency-separation beating and frequency-time broadening, all of which are seen in the received signals. Similar results might be expected to result from coupled multiple ducts like a microduct structure [R. L. Dowden, personal communication (1983)], which consists of smaller enhancement ducts superimposed on a large main duct. This hypothesis is supported both by measurements of microduct-like structures [Mosier, 1976] and by ray tracings in the presence of closely spaced ducts [Strangeways, 1982] which show that energy can be coupled between the ducts.

7. EXPERIMENTAL RESULTS: OTHER FEATURES

Low-Frequency Cutoff

The following are amplitude features of the profiles below f_{-25dB}. In general, the intensity tended to increase with frequency for falling and rising ramps and showed amplitude fluctuations, some of which were noticeably periodic. The intensity did not increase as rapidly as the radiated power rolloff. On rising ramps the intensity was often 5–10 dB greater on rising ramps than on falling ramps for the same

frequency and ramp slope magnitude. Below the nose frequency, dispersion will increase the rising ramp slope magnitude, "squeezing" the wave energy per unit bandwidth into a shorter time period; the opposite will be true for falling ramps. Calculations show that dispersion can adequately account for the intensity difference between the ramps steeper than 1 kHz/s. Since the effects of dispersion are not significant for the more gradual ramps, more data should be examined to see if the observed intensity difference is a repeatable effect.

The −1-kHz/s ramps (e.g., Figure 17) achieved saturation and continued down to low frequencies and radiated power amplitudes (∼1 kHz and ∼10 dB below the respective levels at f_{RG} for the 1-kHz/s ramp) without triggering a free running, rising emission. The grown signal shown in Figure 17 remained locked to the −1-kHz/s ramp until the triggering at ∼2 kHz of free running fallers.

It seems possible that the free running fallers triggered by the −1-kHz/s ramp could be related to low radiated power levels near 2 kHz such that the coherent signal, as it entered the interaction region, could no longer control the emission. An estimate of the applied signal level near the equator at the faller triggering frequency is $B_{eq} \sim 10^{-3}$ pT and $E_{eq} \sim$ 0.01 μV/m. The two fallers shown in Figure 17 (beginning at 1436:42.8 and 1436:43.3) apparently originated on two different paths.

Large differences exist between the radiated power profile and the received signal in the lower cutoff region. If one takes the radiated power profile, subtracts the estimated ionospheric absorption (using the Halley Bay ionograms in this case and calculations up to 1000 km) [Helliwell, 1965], and compares the result with the received amplitude profile, then the difference in the curves represents the contribution from other frequency dependent factors (e.g., wave growth, the coupling into and out of ducts [Strangeways, 1981a, b], and propagation). Such a comparison is shown in Figure 17, top panel. The adjusted radiated power profile was positioned so that it passed through the amplitude-frequency point at which falling ramp growth was inferred to have begun (see previous section). The profile is as much as 50 dB down from the apparently saturated intensity of the received −1-kHz/s ramp. For the other ramps this profile was generally down 20−30 dB from the nonsaturated intensities at frequencies below f_{-25dB}, which could be mainly due to spatial or linear growth. Linear amplification of artificial signals on the order of 20 ± 10 dB was reported by Dowden [1978], and at least 25 dB/hop was reported by McPherson et. al. [1974].

Saturation

The smoothed saturation intensities of the ramps were measured at various frequencies and found to fall within a 10-dB range. This range was centered at −7 dB for the 1436−1441 UT data set and at −15 dB for the 1421−1426 UT data set.

In some cases the saturation amplitude was less than the peak amplitude immediately after growth (e.g., the 0.5-kHz/s ramp, Figure 7a). This "overshoot" was coincident with a spectral broadening during growth which showed frequency fluctuations. This state was not sustained and was followed by a rapid reduction in amplitude coincident with spectral narrowing and reduced frequency fluctuations. The
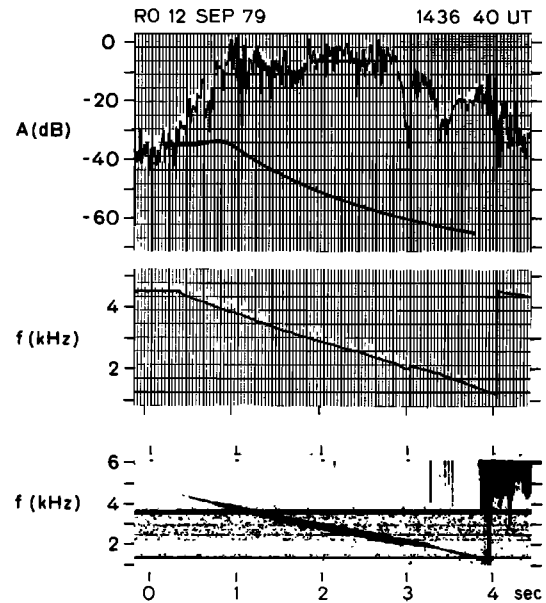

Fig. 17. Details of the −1-kHz/s ramp shown in Figure 2. The top and middle panel are frequency tracking filter, amplitude and frequency versus time curves, respectively. The −1-kHz/s ramp spectra are given in the bottom panel. The radiated power profile, corrected for ionospheric absorption, is given by the solid curve in the top panel.

overshoot phenomenon occurred many times in constant frequency pulses transmitted between 1441 and 1446 UT. On the more gradual ramps, the spectrally broadened signal occasionally continued as a free-running emission (see triggered rising emission section). Following emission triggering, the ramp amplitude was reduced and then, except below f_{RD}, grew back to the saturation level.

Growth Rates

The amplitude profiles of rapid growth are given in Figures 6b, 7a, and 7c. For the purpose of investigating ramp slope dependences, average growth rates measured between the noise level and saturation are given in Figure 18 for the rising ramps of the 1436−1441 UT data set. Because of the unknown influence of the half gyrofrequency ducting loss on falling ramp growth rates and because of local power line harmonic interference on the 1421−1426 UT rising ramp growth curves, growth rates are not given for the other ramps. For the ramps in Figure 18 the growth rate tends to increase as the ramp slope becomes more gradual. These growth rates range from 140 to 40 dB/s, and thus fall within the 25 to 250-dB/s range of several hundred growth rate measurements on constant frequency pulses by Stiles and Helliwell [1977]. The reduced growth rates on the steep ramps could be related to phase equator features such as phase equator spreading, latitudinal variations in the second-order resonant electron number density, and higher phase equator velocities.

Smoothing was used in obtaining the growth rate measurements from the amplitude-time profiles. The variability of amplitude profiles among the ramps and the fluctuations of the amplitude on a given ramp (Figures 6 and 7) were not just due to noise. The repeatability of the period of the
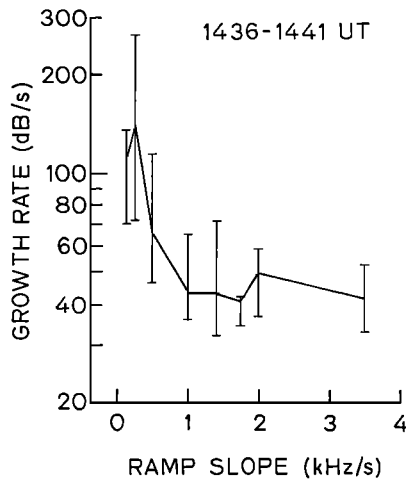
Fig. 18. Exponential growth rates for the rising ramps of Figure 2 measured from the growth curves shown in Figure 7. The error bars represent the maximum and minimum growth rates which could be interpreted from the growth curves.

amplitude fluctuations on different ramps (e.g., the −0.5- and −0.125-kHz/s ramps in Figure 6b) suggests that these were the result of wave-particle interaction rather than some other process such as multipath beating.

Figure 6b suggests that the growth rates within the amplitude range −30 to −15 dB were sometimes greater than the rates between −15 dB and saturation. On the 0.25-kHz/s ramp (Figure 7a), the peak intensity following rapid growth onset was more than 10 dB down from corresponding intensities on the 0.5- and 0.125-kHz/s ramps. This is believed to be due to growth suppression [Raghuram et al., 1977] induced by the diffuse multipath whistler visible in Figure 2.

Triggered Rising Emissions

Triggered emission is a general term used to describe a signal that originates from an input signal and has frequency-time characteristics that differ from those of the dispersed input signal. Figure 2 shows that rising emissions, ("risers") were only triggered by ramps with slope magnitudes less than 1 kHz/s. On some rising ramps, the absence of risers suggests that they cannot be triggered by ramps with slopes exceeding the natural riser slope. The absence of risers on the steeper falling ramps appears to be connected to the lack of saturation in these cases. The apparent saturation on the −1-kHz/s ramp shown in Figure 17 and identified in Figure 8 occurred in a frequency range below that in which risers were triggered on other ramps.

Following the triggering of a riser the ramp intensity was reduced and would then increase. Rates of such regrowth measured on the 1436−1441 UT data set ranged from 79 to 131 dB/s and averaged 83 dB/s for falling ramps and 91 dB/s for rising ramps. Amplitude-time profiles of regrowth were quite similar from case to case (see Figure 7).

The average time between triggered rising emissions tended to decrease with increasing ramp slope. The rising emission is hypothesized to suppress the regrowth of the ramp until the frequency difference between the emission and the ramp becomes greater than about 50−100 Hz. It is also possible that preferential triggering frequencies played a role, since emissions were often seen to be triggered near the same frequency on different ramps.

Associated with the triggering of the last riser on the −0.125-kHz/s ramp (Figure 7d) is a band limited impulse (BLI), a short-lived increase in signal bandwidth. This BLI extends ∼190 Hz above the ramp frequency and is ∼0.04 s in duration, as measured on the amplitude trace.

The following are properties of the rising emissions themselves and represent the "natural" response of the magnetosphere to variable frequency VLF signals. These are given to complement the study of the "driven" response of the magnetosphere to the injection of variable frequency VLF signals.

Independent of the ramp slope and triggering frequency, most of the risers quickly developed a characteristic slope that varied with frequency. Maximum positive slopes ranged from 1.8 to 0.9 kHz/s, while the average positive slope was 0.63 kHz/s. This slope is comparable to the 0.77-kHz/s median slope of 867 rising chorus elements received on OGO 3 [Burtis and Hellwell, 1976].

A rising emission analyzed with a 100-Hz bandwidth tracking filter produced the frequency-time and amplitude-time profiles shown in Figure 19. A maximum slope measurement is shown along with the average overall slope of the measured risers. Rising emissions repeatedly displayed two characteristic modes of behavior, labeled A and B in Figure 19. For mode A, which includes the birth of the emission, the amplitude fluctuates rapidly over a 20-dB range, accompanied by a broadband, speckled, and turbulent appearing spectral signature. For mode B the fluctuation range is less than 10 dB and the spectral signature is relatively narrowband. The transition from mode A to mode B generally coincides with a local minimum in the riser amplitude and discontinuities in the derivatives of frequency with respect to time. Mode B thus begins with regrowth and, in these data, ends with the decay of the emission. These two modes are commonly seen on rising emissions and hooks recorded on other days.

The peak intensity of the risers was generally less than or equal to the peak intensity of the ramps at any given
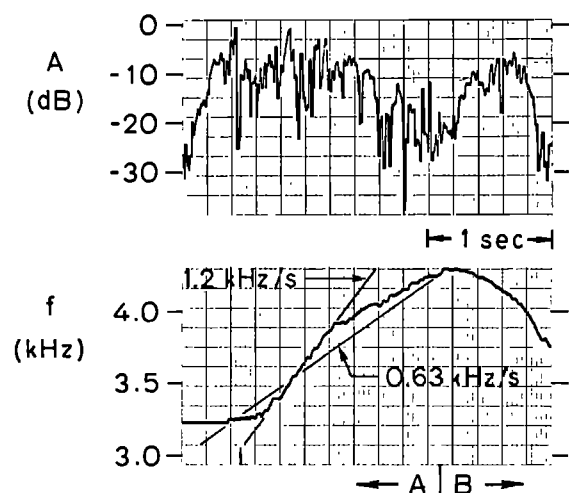

Fig. 19. Amplitude and frequency versus time curves (from a frequency tracking filter) of a rising emission (riser) triggered by the −0.125-kHz/s ramp. Two modes of a rising emission, based on amplitude fluctuations and frequency-time behavior, are identified as A and B, with the tick mark indicating the time of transition. The maximum slope line for this riser (1.2 kHz/s) is drawn along with the average slope line (0.63 kHz/s) for several risers.

frequency. Riser intensities tended to decrease with time (Figure 19). There was also a trend for risers triggered at the high-frequency portion of ramps to rise to higher frequencies than those triggered at lower frequencies (Figure 2).

Magnetospheric Line Radiation or Power Line Harmonic Radiation

There is evidence that rising emissions were influenced by magnetospheric line radiation or power line harmonic radiation (PLHR) [Park and Helliwell, 1981]. Possible riser-PLHR interactions include the termination of risers coincident with PLHR frequencies, preferential triggering frequencies, and possible entrainment of the risers by PLHR. Possible wave-PLHR interactions include the abrupt appearance of a signal at ~2.2 kHz on the 0.5-kHz/s ramp and the lack of received signal between 2.94 and 2.54 kHz on the 3.5-kHz/s ramp (Figure 7a).

8. SUMMARY AND CONCLUDING REMARKS

The magnetospheric response to the injection of coherent variable frequency VLF signals (ramps) has been analyzed, with emphasis upon the results of a particular case study. Ramp slope dependences were found, including (1) upper and lower cutoff effects which varied systematically with ramp slope, and (2) triggering of free running emissions.

Ramp group delay measurements, in conjunction with ionospheric soundings, were used for the first time to yield the L shell, gyrofrequency, and electron density along the whistler mode propagation path. Ramps possess an advantage over whistlers in determining path parameters because of the known location and timing of the transmitted ramp.

A generalized second-order gyroresonance condition, valid for relativistic electrons, was developed in this paper and solved in order to characterize the interaction region, or phase equator. Examination of the phase equator behavior reveals several noteworthy features, many of which, including those given below, are related to dispersion. The concept of the phase equator velocity was developed to describe the change in phase equator location with time, and phase equator velocities greater than the wave or electron velocities were calculated. On falling tones the second-order resonance condition is satisfied at two frequencies for the same electrons, and where the resonance condition is first satisfied, the phase equator splits into two oppositely moving regions. Two phase equators occur at a single frequency for the low-frequency portions of rising ramps, one on the downstream side of the magnetic equator as expected, the other on the upstream side after dispersion of the lower part of the rising ramp into a falling tone. These results suggest that transmitted ramp slope can be varied with frequency to give particular relationships among frequency, phase equator location, and phase equator motion, for given resonant electrons. The use of variable sloped transmissions to control the interaction in a predetermined manner was proposed by Brinca [1981] for cases in which the electron becomes trapped by the wave field.

Another new feature developed in this paper is the spreading of the range of phase equator locations due to the fact that high pitch angle electrons are in second-order resonance

nearer the equator than low pitch angle electrons. The amount of spreading increases with ramp steepness. Associated with this spreading is an asymmetry in the feedback of radiation, with the radiation stimulated by low pitch angle electrons feeding back on the high pitch angle electrons for rising ramps and vice versa for falling ramps. The phenomena of phase equator velocity, phase equator splitting and spreading, the feedback asymmetry in wave growth, and their relations to observable data features require further study. Because these phase equator features might affect the properties of any sustained feedback system, the feedback model of Helliwell and Inan [1982] should be generalized before it is applied to fast ramps or whistlers. The role of feedback and the relative importance of second-order resonance compared to first order resonance in the total wave growth process deserves further study.

The lower cutoff frequency, where rising ramp rapid growth or falling ramp rapid decay occurred, increased as ramp steepness increased. According to our interpretive model, the cutoff corresponds to a critical value of the resonant electron number density, above which temporal growth can occur. This model suggests a hot plasma diagnostic technique in which the observed lower cutoff frequencies are fitted to frequencies at which stimulated magnetic fields pass through threshold values. These threshold values would be calculated using wave-particle interaction simulations with various energetic electron distributions. The technique was tested using a $g(\alpha)v^{-n}$ electron distribution and a simplified wave-particle interaction simulation which considered only second-order resonant electrons. For an isotropic (anisotropic) distribution function, the best fit to the 1421–1426 UT data set gave $n \simeq 5$ ($n \simeq 6$) and the 1436–1441 UT data set gave $n > 10$. The 1421–1426 UT data set and OGO 3 satellite measurements of the differential energy spectrum were consistent with a v^{-5} distribution function. When further developed, this technique could provide a ground-based means of monitoring the magnetospheric hot plasma, complementing the use of non-stationary, satellite-borne particle detectors. A next step toward the development would be to make a detailed statistical comparison of VLF and satellite data. For this purpose, new frequency ramp formats have been designed for transmission from Siple Station.

The upper cutoff features of all the ramps were consistent with a half gyrofrequency ducting loss. Observations of systematic increases in upper cutoff frequencies with increasing rising ramp slope were found to be consistent with a corresponding increase in the half gyrofrequency within interaction regions located off the equator. Falling ramp upper cutoff, occurring at lower frequencies than the rising ramp upper cutoff, was consistent with equatorial ducting loss prior to the arrival of the falling ramp at its upstream interaction region. The upper cutoff could be useful as a hot plasma diagnostic tool when it occurs below the half gyrofrequency; in such cases it could be related to the distribution function rather than to ducting losses.

These interpretations of ramp slope dependences in terms of off-equatorial positions of the interaction region provide the first reported ground based test of Helliwell's [1967] phase equator model. Satellite measurements, also consistent with the model, showed an increase in the ratio of detected rising frequency to falling frequency chorus elements

as the satellite moved nearer the magnetic equator [*Burtis and Helliwell*, 1976].

The upper and lower cutoff data also suggest that the radiated power required to sustain the growth of a signal was often less than the radiated power necessary for the onset of exponential growth, the difference in one case being as much as 10 dB.

The nonsaturated signal intensities at the low frequency limits of the received ramps, when compared with the radiated power profile, indicated that these nonsaturated intensities were 20–30 dB above a calculated unamplified signal level. This difference could be the result of spatial growth and is comparable to spatial growth or linear amplification calculations of 20 ± 10 dB reported by *Dowden* [1978] and at least 25 dB/hop reported by *McPherson et. al.* [1974].

Rising emissions were triggered by ramps with slope magnitudes < 1 kHz/s. The absence of rising emissions on steeper ramps was attributed to a lack of saturation within the frequency range where triggering occurred on the other ramps and to the fact that steep rising ramp slopes exceeded the natural emission slope. A study of the rising emissions revealed two "modes" of repeatable behavior. One mode, which includes the birth of the emission, was characterized by 20-dB fluctuations, accompanied by frequency fluctuations. The other mode was characterized by reduced amplitude fluctuations (<10 dB) and was relatively narrowband.

APPENDIX: THE EQUATIONS OF SECOND-ORDER RESONANCE

At a given point the relativistic condition for first-order resonance is

$$v_{\parallel} \simeq v_R = \frac{2\pi(\frac{f_H}{\gamma} - f)}{k} \qquad (A1)$$

assuming longitudinal propagation. For second-order resonance, the variation of the electron parallel velocity $v_{\parallel}$ along the electron orbit equals the variation of v_R. At a given geomagnetic L shell and latitude ϕ, wave frequency f, and pitch angle α ,the required time variation in f, $[\partial f/\partial t]_{res}$, may be found in terms of known quantities.

The following equation (A2) is a generalized form of the second-order resonance relationship introduced by *Helliwell* [1967] and is valid for longitudinal wave propagation and relativistic electron energies. Adiabatic electron motion is assumed.

$$\left[\frac{\partial f}{\partial t}\right]_{res} = \frac{2cf_H(1 - \Lambda\gamma)[\Lambda(1 - \Lambda)]^{\frac{3}{2}}}{f_p\,(1 + \Lambda\gamma - 2\Lambda^2\gamma)^2} \times \left[\left(3 - \Lambda(\gamma + 2) + (1 - \Lambda(1 + \gamma - \Lambda\gamma))\tan^2\alpha\right)\frac{\partial f_H}{\partial z} - \frac{2f_H}{f_p}(1 - \Lambda\gamma)(1 - \Lambda)\frac{\partial f_p}{\partial z}\right] \qquad (A2)$$

where k, f_p, f_H, and c are the wave number, plasma frequency, gyrofrequency, and velocity of light in free space, respectively. $\Lambda = f/f_H$, $\gamma = (1 - (v_{\parallel}/c\cos\alpha)^2)^{-1/2}$, and z is the field line arc length measured from the magnetic equator in the direction of $\mathbf{v}_{\parallel}$.

The effect of the $\partial f_p/\partial z$ term will only be noticeable at high phase equator latitudes ($|\phi| > 30°$) and can safely be neglected. This term could be significant if the cold plasma

electron density were fluctuating with respect to z [U. S. Inan, personal communication (1984)].

The rate of change of frequency of a propagating (and hence dispersed) ramp at an observing point with geomagnetic latitude ϕ is given by

$$\left[\frac{\partial f}{\partial t}\right]_{res} = \left[\frac{1}{M} + \left[\frac{\partial t}{\partial f}\right]_{iono} + \left[\frac{\partial t}{\partial f}\right]_{\int_{\phi ts}^{\phi}}\right]^{-1} \qquad (A3)$$

where M is the transmitted slope, $[\partial t/\partial f]_{iono}$ is the derivative of the transionospheric group delay and $[\partial t/\partial f]_{\int_{\phi ts}^{\phi}}$ is the derivative of the magnetospheric group delay from the topside ionosphere to ϕ. In this case, the topside ionosphere is the mathematical boundary between the ionosphere and magnetosphere, chosen to be at 1000-km altitude. Using the ionospheric dispersion approximations of *Park* [1972] we have

$$\left[\frac{\partial t}{\partial f}\right]_{iono} \simeq -0.575\sqrt{\frac{N}{f^3}} \qquad (A4)$$

where N is the electron columnar content (el/cm^2) below 1000 km. The magnetospheric term is given by

$$\left[\frac{\partial t}{\partial f}\right]_{\int_{\phi ts}^{\phi}} = \frac{1}{4c}\int_{\phi ts}^{\phi} \frac{f_p f_H (f_H - 4f)}{\sqrt{f^3(f_H - f)^5}}\frac{\partial z}{\partial \phi}d\phi. \qquad (A5)$$

In this paper the second-order resonance latitude ϕ was found by equating the right hand sides of (A2) and (A3) and then applying the "Pegasus" root finding method of *Dowell and Jarratt* [1972]. The N in (A4) was estimated using Halley Bay ionograms.

REFERENCES

Bernard, L. C., A new nose extension method for whistlers, *J. Atmos. Terr. Phys., 35*, 871, 1973.

Bernhardt, P. A., Theory and analysis of the 'super whistler', *J. Geophys. Res., 84*, 5131, 1979.

Brinca, A. L., Enhanceing whistler wave-electron interactions by the use of specially modulated VLF wave injection, *J. Geophys. Res., 86*, 792, 1981.

Burtis, W. J., and R. A. Helliwell, Magnetospheric chorus: Occurrence patterns and normalized frequency, *Planet Space Sci., 24*, 1007, 1976.

Carpenter, D. L., Ducted whistler-mode propagation in the magnetosphere; A half-gyrofrequency upper intensity cutoff and some associated wave growth phenomena, *J. Geophys. Res., 73*, 2919, 1968.

Carpenter, D. L., and Z. T. Bao, Occurrence properties of ducted whistler-mode signals from the new VLF transmitter at Siple Station, Antarctica, *J. Geophys. Res., 88*, 7051, 1983.

Carpenter, D. L., and T. R. Miller, Ducted magnetospheric prop-

agation of signals from the Siple, Antarctica, *J. Geophys. Res.*, *81*, 2692, 1976.

Chang, H. C., Cyclotron resonant scattering of energetic electrons by Electromagnetic waves in the magnetosphere, *Tech. Rep. E414-1*, p. 91, STARLAB, Stanford Electron. Lab., Stanford Univ., Stanford, Calif., 1983a.

Dowden, R. L., A. D. McKay, L. E. S. Amon, H. C. Koons, and M. H. Dazey, Linear and nonlinear amplification in the magnetosphere during a 6.6-kHz transmission, *J. Geophys. Res., 83*, 169, 1978.

Dowell, M., and P. Jarratt, The 'pegasus' method for computing the root of an equation, *BIT, 12*, 503, 1972.

Hashimoto, K., H. Matsumoto, Y. Serizawa, and I. Kimura, Computer simulation of whistler mode wave-particle interactions using a free-boundary encounter model, *J. Geophys. Res., 88*, 3072, 1983.

Helliwell, R. A., *Whistlers and Related Ionospheric Phenomena*, Stanford University Press, Stanford, Calif., 1965.

Helliwell, R. A., A theory of discrete VLF emissions from the magnetosphere, *J. Geophys. Res., 72*, 4773, 1967.

Helliwell, R. A., Intensity of discrete VLF emissions, in *Particles and Fields in the Magnetosphere*, edited by B. M. McCormac, p. 292, D. Reidel, Hingham, Mass., 1970.

Helliwell, R. A., Siple Station experiments on wave-particle interactions in the magnetosphere, in *Wave Instabilities in Space Plasmas*, edited by P. J. Palmadesso and K. Papadopoulos, p. 191, D. Reidel, Hinghan, Mass., 1979.

Helliwell, R. A., VLF wave injection from the ground, Active experiments in space, symposium at Alpbach 24–28 May 1983, *Eur. Space Agency Spec. Publ. ESA, 195, 3*, 1983a.

Helliwell, R. A., Controlled stimulation of VLF emissions from Siple Station, Antarctica, *Radio Sci., 18*, 801, 1983b.

Helliwell, R. A., and U. S. Inan, VLF wave growth and discrete emission triggering in the magnetosphere: A feedback model, *J. Geophys. Res., 87*, 3537, 1982.

Helliwell, R. A., and J. P. Katsufrakis, VLF wave injection into the magnetosphere from Siple Station, Antarctica, *J. Geophys. Res., 79*, 2511, 1974.

Helliwell, R. A., and J. P. Katsufrakis, Controlled wave-particle interaction experiments, in *Upper Atmosphere Research in Antarctica*, Antarctic Res. Ser., vol. 29, p. 100, AGU,Washington, D. C., 1978.

Helliwell, R. A., D. L. Carpenter, and T. R. Miller, Power threshold for growth of coherent VLF signals in the magnetosphere, *J. Geophys. Res., 85*, 3360, 1980.

Kimura, I., H. Matsumoto, T. Mukai, K. Hashimoto, T. F. Bell, U. S. Inan, R. A. Helliwell, and J. P. Katsufrakis, EXOS-B/Siple Station VLF wave-particle interaction experiments: 1. General description and wave-particle correlations, *J. Geophys. Res., 88*, 282, 1983.

Kintner, P. M., R. Brittain, M. C. Kelley, D. L. Carpenter, and M. J. Rycroft, In situ measurements of trans-ionospheric VLF wave injection, *J. Geophys. Res., 88*, 7065, 1983.

Matsumoto, H., Nonlinear whistler-mode interaction and triggered emissions in the magnetosphere: A review, in *Wave In-*

stabilities in Space Plasmas, edited by P. J. Palmadesso and K. Papadopoulos, p. 163, D. Reidel, Hingham, Mass., 1979.

McPherson, D. A., H. C. Koons, M. H. Dazey, R. L. Dowden, L. E. S. Amon, and N. R. Thomson, Alaska to New Zealand whistler-mode transmission at 6.8 kHz, *Nature, 248*, 493, 1974.

Mosier, S. R., Observations of magnetospheric ionization enhancements using upper hybrid resonance noise band data from the RAE 1 satellite, *J. Geophys. Res., 81*, 253, 1976.

Nunn, D., The quasistatic theory of triggered VLF emissions, *Planet. Space Sci., 32*, 325, 1984.

Omura, Y., and H. Matsumoto, Computer simulations of basic processes of coherent whistler wave-particle interactions in the magnetosphere, *J. Geophys. Res., 87*, 4435, 1982.

Park, C. G., Methods of determining electron concentrations in the magnetosphere from nose whistlers, *Tech. Rep. 3454-1*, p. 1, Radioscience Lab., Stanford Electron. Lab., Stanford Univ., Stanford Calif., 1972.

Park, C. G., and R. A. Helliwell, Power line radiation in the magnetosphere, *Adv. Space Res., 1*, 423, 1981.

Raghuram, R., R. L. Smith, and T. F. Bell, VLF Antarctic antenna: Impedance and efficiency, *IEEE Trans. Antennas Propag., AP-22*, 334, 1974.

Raghuram, R., T. F. Bell, R. A. Helliwell, and J. P. Katsufrakis, Echo-induced suppression of coherent VLF transmitter signals in the magnetosphere, *J. Geophys. Res., 82*, 2787, 1977.

Scarabucci, R. R., and R. L. Smith, Study of magnetosperic field oriented irregularities- the mode theory of bell-shaped ducts, *Radio Sci., 6*, 65, 1971.

Schield, M. A., and L. A. Frank, Electron observation between the inner edge of the plasma sheet and the plasmasphere, *J. Geophys. Res., 75*, 5401, 1970.

Smith, R. L., Propagation characteristics of whistlers trapped in field-aligned columns of enhanced ionization, *J. Geophys. Res., 66*, 3699, 1961.

Stiles, G. S., and R. A. Helliwell, Stimulated growth of coherent VLF waves in the magnetospere, *J. Geophys. Res., 82*, 523, 1977.

Strangeways H. J., Determination by ray-tracing of the regions where mid-latitude whistlers exit from the lower ionosphere, *J. Atmos. Terr. Phys., 43*, 231, 1981a.

Strangeways H. J., Trapping of whistler-mode waves in ducts with tapered ends, *J. Atmos. Terr. Phys., 43*, 1071, 1981b.

Strangeways H. J., The effect of multi-duct structure on whistler-mode wave propagation, *J. Atmos. Terr. Phys., 44*, 901, 1982.

Vomvoridis, J. L., T. L. Crystal, and J. Denavit, Theory and computer simulations of magnetospheric very low frequency emissions, *J. Geophys. Res., 87*, 1473, 1982.

C. R. Carlson, D. L. Carpenter, and R. A. Helliwell, Space, Telecommunications, and Radioscience Laboratory, Stanford University, Stanford, CA 94305.